Publications of the Astronomical Society of the Pacific, 129:075002 (18pp), 2017 July https://doi.org/10.1088/1538-3873/aa69b9

Radiation Damage Effects in Space-borne CCD Detectors Operated in TDI Mode

Juan C. Terrazas[1,3,4], L. Corcione[2,4], M. G. Lattanzi[2,4], and M. Gai[2,4]
[1] Departamento de Ingeniería Eléctrica, Facultad de Ciencias Físicas y Matemáticas, Universidad de Chile; jterraza@das.uchile.cl
[2] Osservatorio Astronomico di Torino (OATo), Turin—ITALY; corcione@oato.inaf.it, lattanzi@oato.inaf.it, gai@oato.inaf.it
Received 2015 December 31; accepted 2017 February 17; published 2017 May 25

Abstract

We evaluate the astrometric and photometric implications of a series of laboratory tests conducted to study the effects of radiation damage caused by solar protons in space-borne charge coupled devices (CCDs). The photometric effects, i.e., charge loss (CL) and the astrometric effects, i.e., location biases, associated with the radiation-induced distortion on the sampled line spread function (LSF), are assessed via a Gaussian fitting model. Data reduction is supported by a detailed analysis of the experimental setup. Charge loss and centroid shift variations are evaluated as functions of the simulated star brightness and the level of diffuse optical background to derive useful hints for modeling and calibration of the radiation damaged LSF during actual payload operations in orbit.

Key words: techniques: photometric – CCD – instrumentation: detectors – methods: data analysis

1. Introduction

The present work makes use of laboratory radiation tests developed to study properties of the imaging payload that has been working effectively since 2013 December 19, onboard the *Gaia* Satellite, which will be subjected throughout its operational lifetime to environmental conditions of the region around the Lagrangian point L2 of the Sun-Earth system (Gaia Collaboration 2016), affecting the measurement of radial velocities, proper motions, and parallaxes of over one billion stars.

1.1. Gaia Mission

Gaia is a cornerstone mission of the European Space Agency (ESA), which uses a measurement scheme similar to its predecessor *Hipparcos* (Perryman et al. 2001), to build an extraordinarily precise three-dimensional (3*D*) map of the positions and motions of about one billion stars in our Galaxy.

Gaia implements a 4π sky survey from an orbit around the Lagrange point L2 placed at about 1.5×10^6 km from Earth, by simultaneously imaging two fields of view separated by a highly stable and large angle of $106^{\circ}.5$ (basic angle).

Crowley et al. (2016) presents a description of the actual *Gaia* focal plane assembly (FPA), which is basically made of a mosaic of 106 large format (4500 × 1966 Pixels) CCD detectors and is functionally split as follows (see Figure 1): the Sky Mapper (SM) CCDs detects the photons entering the field of view and computes the position of subsequent readout windows; the astrometric field (AF) CCDs performs the exposures devoted to astrometric measurements; the blue and red photometer CCDs provide spectro-photometric measurements of low resolution in the spectral ranges of 330–680 *nm* and 640–1000 *nm*, respectively; the radial velocity spectrometer (RVS) provides moderate resolution spectra for objects brighter than 17th magnitude; wave front sensors (WFS); and the basic-angle monitor (BAM) devices are used for the initial instrumental setup and to monitor the evolution of key instrumental parameters during the mission.

For payload and onboard calibration subsystems, the interested reader can consult the *Gaia* mission portal at http://www.esa.int/Our_Activities/Space_Science/Gaia.

Because radiation damage was considered potentially critical to the space mission, several relevant test campaigns were performed to investigate their consequences. Therefore, the laboratory experiment reported in this article was focused on the usage of diffuse optical background (DoB) as a possible alternative to minimize the impact of radiation damage to the photometric and astrometric performance of the FPA.

2. Radiation Environment

ESA's *Gaia* space mission is projected for a five-year operational lifetime at L2, where it is subjected to the radioactive environment composed of a complex spectrum of natural space radiation that includes solar wind plasma (95% protons, 5% He^{++}) and ionizing radiation (i.e., energetic electrons; ions; protons and alpha particles from solar flares coronal mass ejections; and Jovian electrons). Some contributions are more or less continuous (cosmic rays), whereas others

[3] Departamento de Ingeniería Eléctrica, Facultad de Ciencias Físicas y Matemáticas, Universidad de Chile, Beauchef 850, Santiado de Chile.
[4] INAF-OATo; Osservatorio Astronomico di Torino (OATo), Via Osservatorio 20 I-10025 Pino Torinese, Turin—ITALY.

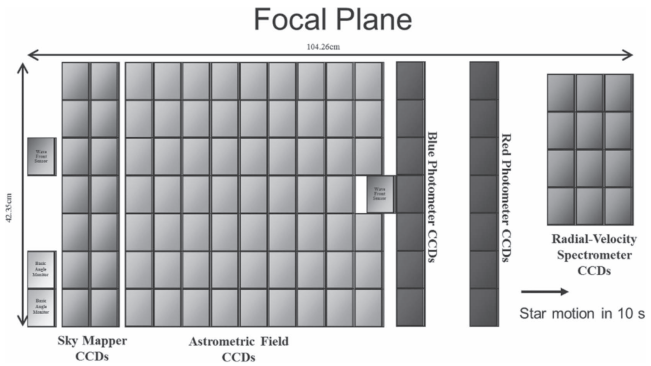

Figure 1. The focal plane assembly consists of two fields of view (telescopes) mapped onto a common focal plane made of 106 large-format CCDs, each with 4500 TDI lines, 1,966 pixel columns, and pixels of size 10 μm along scan (AL) $\times$ 30 μm across scan (AC) (59 mas $\times$ 177 mas on sky). Star images cross the focal plane in the direction and are indicated by the arrow, AL vs. AC. The focal plane is distributed in: 14 sky mapper CCDs, 63 Astrometric CCDs, 7 blue photometry and 7 Red photometer CCDs and 12 Radial velocity spectrometer CCDs. (Image credits: ESA/*Gaia*, retrieved from ESA/Gaia (2017).)

feature sudden peaks (i.e., solar flares) as can be seen in the work of Daibog et al. (2013).

Gaia works with one of the most complex CCD mosaics ever built, designed and manufactured by e2v technologies (UK), (cf. Section 1.1, which introduces a brief description of the FPA).

Each CCD in the *Gaia* focal plane fulfills different astrophysical functions such as astrometry (i.e., parallaxes, positions, and proper motions), photometry (i.e., magnitudes) spectrophotometry (i.e., stellar temperatures, gravities, metallicity, etc.) and spectroscopy (i.e., radial velocities).

The radiation environment where the focal plane (Figure 1) operates is a critical factor, which can seriously restrict the performance of the *Gaia* CCDs. The local interplanetary environment can essentially be considered dominated by solar flare protons (see Hopkinson & Mohammadzadeh 2003 and Prod'homme et al. 2012) whose most critical damage to the *Gaia* CCD's occurs in terms of non-ionizing or displacement damage (NIEL) that is associated with the generation of electron traps such as solar protons that pass through the epitaxial silicon, colliding with silicon atoms, and displacing them from their locations in the silicon lattice.

Disruption of the crystal lattice introduced by spurious energy levels in the semiconductor band gap are responsible for photoelectron trapping and de-trapping. Note that the traps can belong to diverse species defined by the parameters described according to the Shockley-Read-Hall (SRH) formalism.

Thanks to the time and delay integration (TDI) readout mode, there are statistical processes of electron capture and release that occur with different time constants, depending on the trap species and their activity (Raison & Martin-Fleitas 2009). This could drastically affect all the *Gaia* photometric, astrometric, and spectroscopic measurements with its respective errors due to charge loss, charge release, and deformation of the image profile.

The (minimal) shielding offered by the large *Gaia* focal plane assembly (FPA) reduces the NIEL dose to an expected level that should not exceed 10 MeV protons/cm^2 (see Seabroke et al. 2009 and Fusero et al. 2007). Analogous studies were presented for the satellite missions XMM and CHANDRA (See Meidinger et al. 1996 and Prigozhin et al. 2000)

Gaia CCDs are endowed with features specifically aimed at reducing the effects of radiation-induced charge traps. The pixel architecture incorporates a supplementary buried channel (*SBC*) that reduces the interaction cross section between small electron packets and traps. The CCDs also have a charge injection (CI) structure on the top of the parallel registers to periodically supply calibrated amounts of electrons into the pixels, so as to fill and make inactive almost all the radiation-induced traps before the transit of the stars.

Note that the *Gaia* CCD is a four-phase CCD. The device chip is custom designed to look down in the electronic matrix scheme (i.e., back-illuminated). The CCD sensor comprises 1966 columns with 4500 active pixels, clocked continuously to give a time-delay integration (TDI) operation. A more detailed description can be found in Walker et al. (2008)

Besides design solutions for improving (CTE), other countermeasures were considered for in-flight operations to mitigate the radiation damage effects, such as the adoption of a suitable level for the DoB and CI to fill the charge traps. The potential benefit of both has been assessed through laboratory tests together with the real consequences of the radiation damage.

This paper presents an independent analysis of the radiation test campaign CCN10 executed by EADS Astrium (Toulouse, France) under the ESA contract. The aim is to characterize charge loss, proxy for photometric bias (Corcione et al. 2009), and centroid bias, the analog for astrometry (Terrazas et al. 2010), as functions of signal brightness.

Our analysis provides empirical evidence for calibrating radiation damage models that could be employed for bias removal during processing of the *Gaia* data.

The specific goals of this analysis are

- to measure the PSF centroid (location), shift (bias) and charge loss as a function of signal level;
- to investigate the possible mitigating role of applying DoB; and
- to provide experimental evidence toward the development of mathematical models (and algorithms) to simulate and possibly calibrate the effects of radiation damage consequences.

Section 2.1 presents details of our data reduction model, as well as the approaches employed. Results of the data analysis are presented in Sections 4.2 and 4.3, which describe the

Table 1
Notation Used in this Paper According to the Acronyms Utilized by the Online *Gaia* Acronym Database Maintained by de Bruijne (2016)

Acronym	Name Description
AC	Across scan
AF	Astrometric field
AL	Along scan
BA	Basic angle
BAM	Basic angle monitor
CCD	Charge coupled device
CI	Charge injection
CL	Charge loss
CTE	Charge transfer efficiency
CTI	Charge transfer inefficiency
DoB	Diffuse optical background
EP	Energy particles
FPA	Focal plane assembly
GCR	Galactic cosmic rays
IZ	Irradiated zone
IT	Irradiated test
LSF	Line spread function
NIZ	Non-irradiated zone
PSF	Point spread function
RefT	Referential test
RVS	Radial velocity spectrometer
RTC	Radiation test campaign
SBC	Supplementary buried channel
S/N	Signal-to-noise ratio
SM	Sky mapper
TDI	Time and delay integration
TZ	Transition zone
WFS	Wave front sensors
3D	Three-dimensional

consequences of CTI degradation and, also, the bias distortion induced by radiation damage suffered in the astrometric and photometric measurements.

2.1. Radiation Test Campaign: CCN10

A full description of the test setup is given in internal reports of EADS-Astrium according to the specific features suggested by the manufacturer company (e2v), and we will recall the relevant features of the experiment, as well as some characteristics of the astro focal CCD (AFCCD) Table 1 lists the respective terms and technical abbreviations used in this article.

The global approach to the CCD operation conditions, test facilities, and different procedure modes implies controlling during the radiation tests campaigns (RTC) performed at 165°K and controlling noise measurement in the full frame mode.

The RTC strategies search to mitigate the impact of radiation damage and reduce pernicious effects during the operational life of the Gaia satellite. Following this line of research, the first RTC called CCN10 was performed by Sira and EADS -Astrium, which studies the fundamental physical limits

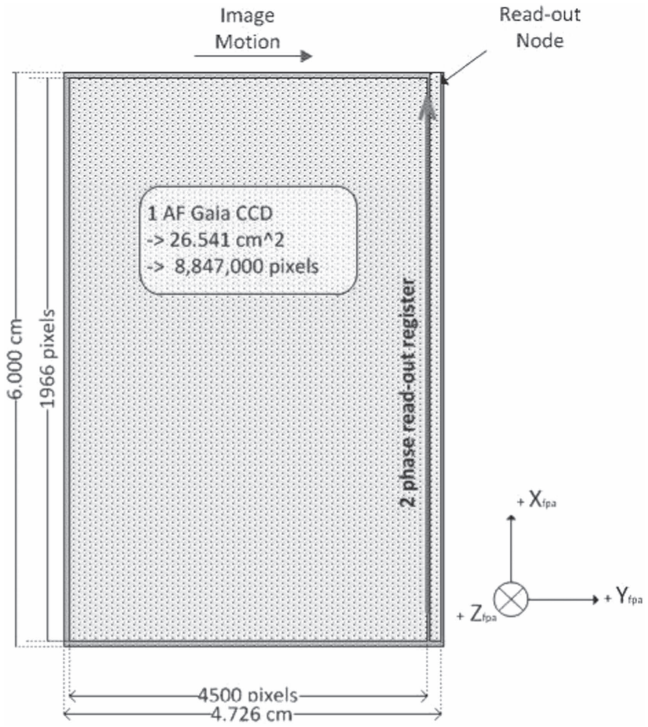

Figure 2. Astro CCD scheme, single CCD.

generated by traps and reflected in astrometric bias and photometric charge loss. Note that RTC CCN10 was the first study open to the *Gaia* community that included a small mask and the use of DoB.

Successive experiments (not presented in this manuscript) were executed using charge injection (CI) termed RTC 2 which works under different configurations and voltages and includes a larger and complex optical mask, as well as RTC 3, carried out using DoB and CI together (see Pasquier et al. 2011).

On the other hand, similar radiation tests were executed for the photometric and RVS CCDs retaining the same RTC setup conditions. The results of these studies were studied in depth and evaluated by the radiation task force at the DPAC—*Gaia* consortium meetings before the launch of the satellite.

Sections 3.2 and 4.2 describe the analysis of the RTC CCN10 at diverse levels of DoB over six different intensity fluxes studying the radiation-induced charge loss and centroid bias effect. Note that the RTC CCN10 has an equivalent fluency dose of 10 MeV protons which for the purpose of this experiment represents the expected radiation dose that *Gaia* could face throughout the entire mission.

The CCN10 test was carried out with a typical *Gaia* CCD (Figure 2), which had been previously exposed to proton irradiation of different intensities across two zones of the CCD (Figure 3(a)), in accordance with an irradiation scheme agreed upon by ESA and EADS Astrium. Following the across scan direction (AC) (from top to bottom), one-third, or about 600

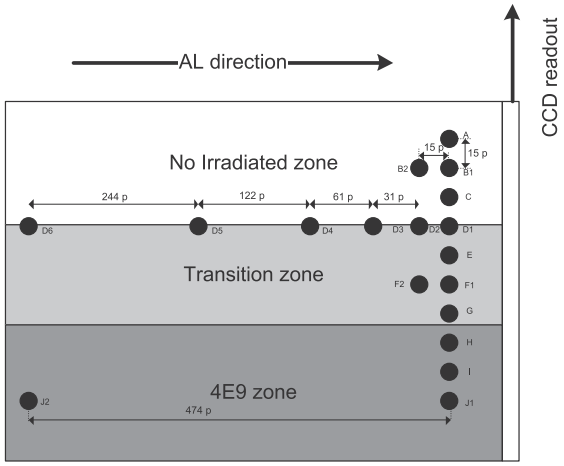

(a) CCN10 mask pattern design

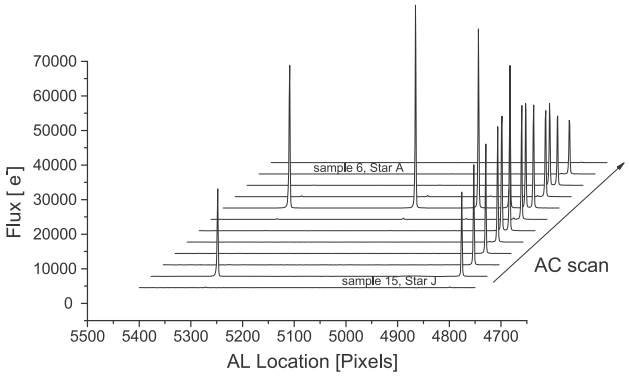

(b) LSF location (AL and AC for a single run), each run has 6500 TDI over 4500 real pixels

Figure 3. (a) CCN10 mask pattern configuration. Note that this figure shows the along scan (AL) location of the pseudo-stars when the mask is placed over the three zones of CCD, whereas (b) illustrates the mask plotted from the corresponding readout data.

lines (i.e., 20 mm in size), of the CCD sensitive area was kept shielded from proton radiation by an aluminum plate, the middle section of the same size, from line 650 to line 1.250, received a 4×10^9 protons/cm^2 equivalent dose, that corresponded to the predicted amount of 10 MeV protons received by the end of the five-year operational life, the remaining 20 mm length AC, from line 1400 to line 1966 was irradiated at a level of 10×10^{10} protons/cm^2.

In between zones, there is a *transition area*, where the radiation level changes progressively in an unpredictable way. The CCD operates electrically and thermally in nominal flight conditions. Laboratory measurements were taken at 165°K, simulating pseudo stars (PSFs) using an optical mask (Figure 3(b)) with 14 pinholes (Figure 3(a)) arranged in two columns, which were aligned almost orthogonally across scan (AC) to the TDI motion versus along scan (AL). Note that our analysis only employs the 10 leading pinholes of the first column; the spots are labeled by astrium from A to J (Figure 3(a)).

The data set comprises 20 TDI transits of the mask for each of six signal levels, corresponding nominally to 60,000, 7000, 2000, 650, 400, and 200 e^- (see Table 2), integrated along a CCD transit (i.e., 4500 TDI steps = 4.42 s), the *Gaia* TDI readout mode works with a pixel frequency of 80 KHz for the image area and of 400 KHz for the readout register.

According to the applicable *Gaia* configuration, the adopted signal intensities would span a magnitude range from $V = 13$ (test performed at 60,000 e^-) to $V = 22$ (test at 200 e^-). Measurements at each signal level were repeated for three different levels of DoB, namely, at levels of 0, 5, and 10 e^-/pixel.

During each TDI transit, the mask (Figure 3(a)) was placed in front of the CCD covering a strip of parallel registers ranging from the non-irradiated zone (NIZ) to the 4×10^9 protons/cm^2 irradiated zone (IZ). Light spots *A*, *B*, *C*, and *D* transited over the NIZ, while spots from *E*, *F*, and *G* passed over the Transition Zone (TZ) between the NIZ and IZ; spots *H*, *I*, and *J* passed entirely over the 4×10^9 irradiated zone and pseudo star "D" slightly overlaps NIZ and TZ (see Figure 3(a)), so it is expected to experience partial irradiation.

A set of 20 TDI transits are executed according to each flux level. For calibration purposes an independent data test was executed where all the PSFs are placed in the NIZ, the flux of approximately 60,000 e^- is hereafter denominated as reference data test (RefT).

Each PSF is individually spread over a 15×15 pixel window and binned across scan at the CCD readout node, so a total of 380 PSFs are individually simulated line spread functions (LSFs), 15 pixels AL, Figure 3(b)) and need to be fitted per each measurement session with a given intensity signal and DoB level.

Gaia RTC CCN10 reports that RefT and IT were executed under the same laboratory conditions, implementing the operation and thermal process at 165° K (established by GAIA consortium for space satellite operation). During the performance of RTC the temperature drift during 20 runs in each session was smaller than 1° K.

Summarizing the setup condition for the whole RTC CCN10, we have:

1. CCD is irradiated before the radiation test campaign is performed.
2. CCD has three regions, two of which are damaged, and in between each region there is a TZ.
3. RefT were obtained placing the complete optical mask in front of the NIZ region where all the pseudo stars of the mask had an illumination level around 60,000 e^- without DoB. After that, the mask is relocated in front of the three regions investigated i.e., NIZ, TZ, and IZ, and the RTC is

Table 2
Radiation CCN10, Chronological test Schedule

DoB = 00		DoB = 05		DoB = 10	
Flux	Date	Flux	Date	Flux	Date
S = 7000	05/04/2006	S = 2000	16/05/2006	S = 200	17/05/2006
S = 2000	05/04/2006	S = 7000	16/05/2006	S = 400	17/05/2006
S = 650	05/04/2006	S = 60,000	16/05/2006	S = 650	17/05/2006
S = 400	05/04/2006	S = 200	18/05/2006	S = 2000	17/05/2006
S = 60,000	14/04/2006	S = 400	18/05/2006	S = 7000	17/05/2006
S = 200	05/05/2006	S = 650	18/05/2006	S = 60,000	17/05/2006
Non-irradiated test					
RefT	11/04/2006				

executed. Figure 3(b) shows the luminance trend distribution of the mask brightness.

4. RTC CCN10 simulates the CCD response for diverse stellar magnitudes at three different levels of DoB (i.e., 0, 5, and 10).
5. Unfortunately, the first TZ (between NIZ and IZ) is not well understood, and there is no way to characterize the condition under which radiation degrades this region of the CCD.

All the tests reported in Table 2 were executed a month apart. We can assume that different features of the analysis and results may have been compromised due to temporal variations, and it is crucial to know the thermal and electrical conditions of the CCD between sessions. However, this fact gives the option to see the photometric and astrometric efficiency of the CCD when the device is permanently damaged, even considering different fluxes, DoB, and time.

3. Measurement Analysis

3.1. Measurement Model

Different alternatives exist to perform an analysis of the radiation test campaign. For example, a non-parametric approach based on the Cramer–Rao Lower Bound (CRLB) proposed by Mendez et al. (2014) allows us to study the lower variance error associated with the astrometric measurements. Our analysis, however, adopts the Gaussian function (Equation (1)) to study the stellar photometry and astrometry effects,

$$y = y_0 + \frac{A_0}{\sigma\sqrt{\frac{\pi}{2}}} e^{-2\frac{(x-x_c)^2}{\sigma^2}}, \quad (1)$$

where the fit parameters are:

y_0 = Brightness offset that calculates the background counts under the PSF;
x_c = PSF Centroid location;
σ = Standard deviation; and
A_0 = total area under the curve above the background (i.e., integral flux).

Our Gaussian model is not the most accurate mathematical function for damaged image profiles; however, all we need here is a simple and robust estimator suitable for accurately comparing estimated image parameters (location and integral flux, in particular) from both RefT and IT data. Therefore, the adoption of the Gaussian function is certainly up to the task.

The Gaussian spot brightness (integral flux) from the RefT is used to calibrate the brightness from the irradiated session so as to compensate for the signal variation across the mask due to the light source distribution. Note that a fundamental problem is associated with radiation-induced charge transfer inefficiency ($CTI = 1 - CTE$), which is computable from the calibrated brightness spots of the RefT and the first three pinholes of the IT confronted with the spots in the TZ and IZ of the CCD parallel registers. More detailed information will be presented in Section 3.2 where all the mathematical steps used to calculate the respective photometric charge loss are described.

Concerning the astrometric calibration, the Gaussian centroid location is first used to fit RefT data to investigate the repeatability of the experiments and to assess the tilt and distortion of the centroid bias related to the opto-mechanic setup, or "mask bias". The centroid bias associated with the radiation damage is then obtained by first linking the Gaussian centroid positions from the LFS samples in the irradiated region of the CCD to the reference centroids from the non-irradiated LSF samples, then correcting the results for the mask bias; this analysis is presented in Section 3.3.

The availability of different experimental sessions executed with differing signal intensities and DoB levels allows us to eventually correlate the charge loss and centroid (location) bias with the signal strength and the added background signal and to also assess the role of DoB against radiation damage (see Section 4.3.).

Table 3
S/N for DoB = 0 Sessions

Star	$S = 200$	$S = 400$	$S = 650$	$S = 2000$	$S = 7000$	$S = 60{,}000$
A	7.12	15.33	18.20	35.41	64.29	190.09
B	9.38	18.04	21.07	40.95	73.65	216.73
C	10.50	19.75	23.68	45.16	80.61	237.36
D	11.21	21.16	25.30	47.62	85.54	251.18
E	10.72	20.16	25.54	47.16	85.15	252.77
F	9.31	18.27	24.76	44.35	80.07	236.94
G	8.27	16.10	23.40	40.32	72.52	211.75
H	7.49	15.26	22.74	38.66	69.80	201.38
I	7.00	14.69	21.20	36.75	66.80	191.55
J	6.43	12.60	19.17	33.08	61.04	176.97

3.2. Photometric Analysis

The average spot intensities from the Gaussian fit (i.e., the Gaussian area of each spot averaged over the number of transits) are first used for a quick check of the data set. We recognize that charge loss affects the spot signal across the damaged area, therefore we need to study the DoB effectiveness in healing the radiation damage. Such a preliminary analysis also serves to understand how to properly calibrate spot brightness for a more detailed investigation of the relationship between charge loss, spot intensity and DoB.

A first goodness check was accomplished by computing the LFS profile contrast, i.e., the signal-to-noise ratio (S/N) for all leading image spots:

$$SNR = \frac{A_0}{\sqrt{n_{signal} + (V\ ar_{Backg} * 15)}} \quad (2)$$

The S/N adopts as a source signal the integral of the Gaussian fit, where A_0 is the integral area under the Gaussian fit and the total noise is the sum of the Poisson noise of the source and the background noise.

The background noise associated with the source is the product of the statistical variance of the background times the quoted source size (i.e., 15-pixel LSF window). We understand that the square root of the variance $V\ ar^{1/2}_{Backg}$ is equal to one standard deviation, or the *rms*, of the signal over the first 4,500 TDI steps preceding the simulated star imprints, and it includes the background signal of photon noise and the electronic readout noise (RON).

The S/N estimates over all the total irradiated data set are shown in Tables 3, 4, and 5, respectively. All the LSF profiles are well above the detection threshold (i.e., S/N = 3), even at the lowest light exposure equivalent to ($S = 200$) electrons.

The S/N is mainly dominated by the signal power, and the extra noise contribution from the DoB (integrated over the $15 \times 15 -$ pixel signal window) is the main reason for the noticeable decrease of the S/N from the null DoB case down to the DoB = 10 case, which affects the measurements at every illumination level from $S = 200$ to $S = 60{,}000$.

As the signal level increases and the background noise contribution become less relevant, the measurements approach the photon noise limited regime and S/N values get very close to the square root of the star signal. This trend applies to all measured leading spots regardless of the illumination signal power. Spots *D*, *E*, and *F* are always within the photon noise limited regime because the most significant flux distribution across the mask is reached by the peaks close to the pinholes *D* to *E*.

Such a feature of the brightness distribution is common for every flux measurement test (see Figure 4), which could likely be associated with the optical setup of the experiment actually affected by a non-uniform illumination across scan as also observed in Figure 3(b).

The comparison of the scan-averaged Gaussian brightnesses from different test sessions reveals a lack of stability in the external light source, observed in different DoB sessions. Note that RefT in each of Figures 4(a) and (b) includes the respective nominal and equivalent illumination levels in the experiments.

Figures 4(a) and (b) draw a first view of the photometric signature for each flux level, where the flux tendency is more discernible for cases with $S = 60{,}000\ e^-$ (See Figure 9) under diverse DoB. Observe that the flux intensity trend at each nominal level changes along IZ due to radiation-induced CTI, like in the case with DoB = 5, not presented in the graphics panel of Figure 4 but discussed in more detail below in Section 4.2.

As we observe in Figure 4 for brightest sessions with flux intensities over $S \geqslant 2000\ e^-$, CTI is reflected as a low illumination trend (pseudo-stars placed in the IZ) with respect to the tendency derived from the spots placed in the non-irradiated region (see Figure 4 for DOB of 0 and 10, respectively). However, RTC of fainter signal levels ostensibly do not reveal any charge loss signature in the photometric curves even under the influence of DoB. However, as we shall see in Section 4.2, we extend the study of charge loss actions along the RTC CCN10.

Figure 5(a) shows the photometric loss of the first scan with respect to the average. It is therefore very instructive to investigate the charge loss that occurs scan by scan, at least for

Table 4
S/N for DoB = Five Sessions

Star	$S = 200$	$S = 400$	$S = 650$	$S = 2000$	$S = 7000$	$S = 60{,}000$
A	6.10	11.18	15.21	35.56	69.08	214.83
B	7.77	13.72	18.13	41.62	78.69	244.88
C	8.65	17.18	20.74	46.08	86.22	268.66
D	9.49	17.18	22.40	49.36	91.66	284.63
E	9.90	17.39	22.57	50.38	93.29	288.58
F	9.19	17.15	21.81	48.67	90.07	275.83
G	8.70	15.63	20.24	45.87	84.67	253.57
H	8.02	14.90	19.50	44.11	81.65	241.98
I	7.65	13.67	18.00	42.18	78.06	228.87
J	6.86	12.18	16.16	37.48	69.87	210.44

Table 5
S/N for DoB = Ten Sessions

Star	$S = 200$	$S = 400$	$S = 650$	$S = 2000$	$S = 7000$	$S = 60{,}000$
A	4.94	12.92	16.84	28.40	64.41	202.35
B	6.27	15.62	19.36	34.21	73.70	230.83
C	6.99	17.06	22.07	38.25	80.86	253.35
D	7.74	18.56	23.69	41.00	85.91	268.54
E	8.11	19.20	24.02	42.30	87.44	272.01
F	7.44	18.82	23.62	41.64	85.13	257.65
G	6.98	18.15	22.88	39.18	79.97	236.50
H	6.47	16.22	21.36	37.33	77.41	226.72
I	6.13	15.74	20.38	35.16	73.91	215.50
J	5.42	13.66	18.03	31.28	67.80	197.33

the brightest sessions $S = 60{,}000$, $S = 7000$, and 2000 e^- showing a measurable signature of trap activity.

The first analysis involves differences of the Gaussian spot brightness in every scan with respect to the value in the preceding scan:

$$S_F = S_n - S_{(n-1)}, \tag{3}$$

where S_F typifies the charge loss and reveals the trap activity run after run. The outcomes are shown in Figure 5(b) for 60,000 e^- cases (with null DoB). Equation (3) also avoids any possible mitigation from the extra background signal, as shown in Figure 5(a), where the flux differences of simulated stars in the non-irradiated area (*A*, *B*, and *C*) are close to zero (Figure 5(b), black square), confirming that this region is not affected by radiation damage.

Star *D* (Figure 5(b)) is located along the edge of the NIZ and the TZ, which seems to reveal a moderate trap activity in between the first and second run, whereas trap effects of radiation damage increase progressively higher along the TZ (stars *F* and *G*). Finally, stars *H*, *I*, and *J* are fully embedded in the irradiated zone.

The amount of charge loss for stars over the irradiated area and in the transition zone is strongly correlated with the signal intensity. The image spots from *E* to *J*, spanning over the transition zone and the irradiated area, undergo a further reduction of charge, though smaller, between the second to third passage. After the third run, the statistical fluctuations of the residual trailing charge for the perturbed stars is noisier than the ones associated with undamaged stars *A*, *B*, and *C*, likely a consequence of stochastic processes of release and capture of charge taking place in between runs. The trap activity affects also the experiment with $S = 2000$ and $S = 7000$; although in this case measurements are heavily dominated by signal fluctuation among scans (Figure 5(b), lower panel).

The charge loss behavior scan after scan reveals the healing role of self-injection by which the charge injection into damaged pixels due to the first transiting stars paves (Figure 5(b)) the way to stars in subsequent scans, which are no longer (or much less) affected by traps. This is likely a consequence of the fact that most of the traps are "slow" traps featuring a typical release time constant longer than the 30 *sec* interval between scans.

Bebek et al. (2002) also observes that CTE follows the temperature tendency and radiation trap effects are present in the first scan reflecting the influence of CTI. Similarly, Short et al. (2010) mentions that a loss of charge during photon

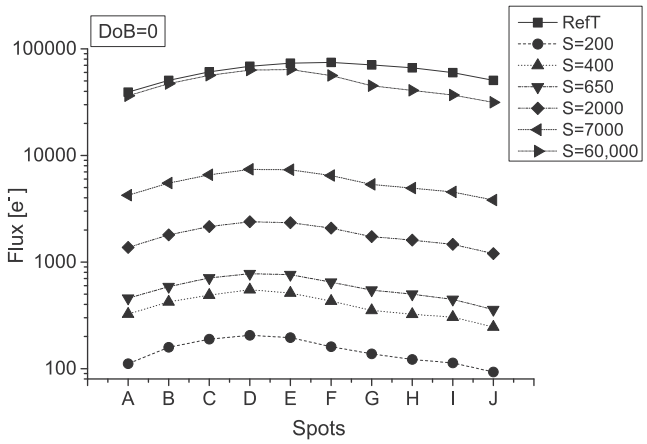

(a) CCN10 mask Brightness DoB=0

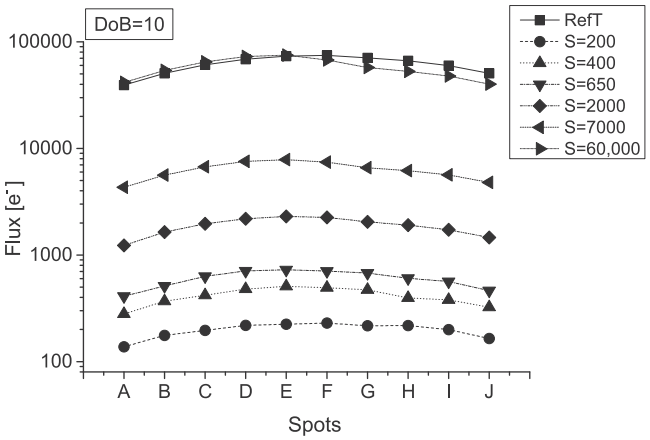

(b) CCN10 mask Brightness DoB=10

Figure 4. Figures 4(a) and (b) show the mask brightness trends for CCN10 DoB = 0 and DoB = 10 tests respectively. Data uncertainties are too small to be plotted within ranges of: 59−300 e^- over 60,000 e^-. Note that the black square points represent the RefT of the NIZ, whereas the remaining symbols belong to each IT test over all the Fluxes.

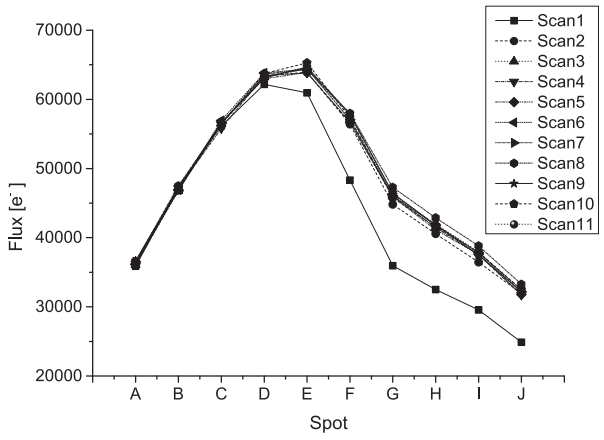

(a) Brightness flux: 600000 e^- RTC CCN10 DoB = 5

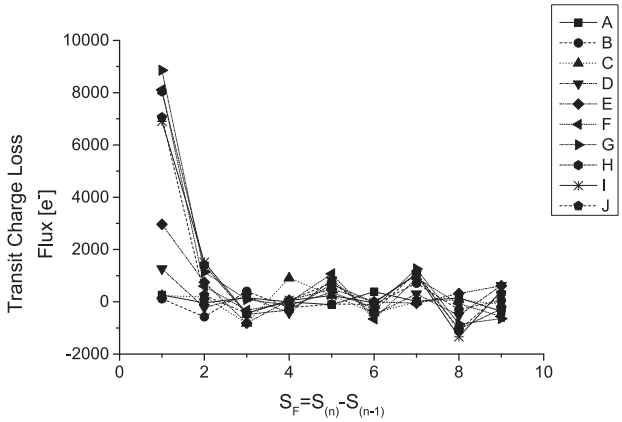

(b) Charge release signature scan after scan RTC CCN10 DoB = 5 for $S = 60000$ e^- under TDI mode.

Figure 5. (a) reveals how the traps remain filled mostly expressed in charge loss between the first scan (black square) and the other exposures (mean scans), whereas (b) illustrates the charge release signature scan after scan; these results makes visible the activity of the traps illustrating the achievement of the chip performance after each transit.

collection and transfer is observed as a consequence of radiation after the second scan.

On the other hand, the non-uniform illumination across the mask and the light source fluctuation during test sessions need to be compensated by an appropriate brightness calibration to achieve meaningful evaluation of the radiation-induced charge loss. The photometric calibration is performed by the flat-fielding method (Equation (4)) which averages the Gaussian brightness of the equivalent measurements for every star signal. Such is the case of IT where each star signal is divided by the corresponding value from the RefT and the result is re-scaled to the mean brightness across the mask of the RefT:

$$S_i^{cal} = \frac{S_i}{S_i^{ref}} \times \widehat{S}^{ref}. \quad (4)$$

Flat-fielding results for all illumination levels are shown in Figures 6(a), (b), and (c) for sessions with DoB = 0, DoB = 5, and DoB = 10, respectively. The calibrated brightness distribution across the mask for all the illumination levels are shown in logarithmic scale; the left panels illustrate fainter sources, whereas right panels compare the brightest sources.

Section 4.2 explains the characterization of the percentage charge loss for the nominal illumination flux intensities of $S = 7000$ and $S = 60{,}000$, with DoB = 0. Measurements reveal a 35% decrease in the photon charge loss generation as compared to the RTC with DoB = 5 and DoB = 10, which display a 25% degradation in charge counting.

At low illumination levels from $S = 200$ to $S = 2000$, the brightness levels for the three DoB sessions are comparable. The most noteworthy difference between sessions consists in a

drop of the signals for image spots *H* through *J* passing over the 4×10^9 IZ with respect to the mean signal of spots *A* through *C* in the NIZ.

For the null DoB session, the signal drop, i.e., CTI charge loss signature is clearly measurable at all illumination levels. As the background increases, the signal variation across the mask significantly reduces for all illumination levels and almost vanishes at a very low signal regime (Figures 6(b) and 6(c), left panels): measurements for DoB = 5 session with $S = 200$ show a very marginal but still clearly measurable signature of the trap activity in the irradiated region. At the equivalent illumination level but with DoB = 10, the trap effect is less evident and the charge loss signature is more ambiguous. We assume that charge loss is still present but covered by noise.

The response of the CCD irradiated region is further discussed in Section 4.2 through quantitative evaluation of the charge loss across the mask and as a function of the signal intensity.

3.3. Mask Centroid Bias: Tilt and Distortion

As it was previously explained in Section 2.1 the data set "RefT" was obtained from execution of the test over the entire NIZ of the CCD during the first part of the CCN10 RTC, involving a sequence of 20 passages of the mask over the CCD with nominally non damaged pixels at a signal level close to 60,000 e^- and null DoB.

These data allow us to assess the Opto-mechanic features of the experiment such as the tilt angle of the mask and the mechanic jitter, which are crucial for characterization and accurate calibration of the centroid bias ultimately related to the radiation damage. Therefore, it is very important to investigate the repeatability of the mask position on the CCD and whether this could possibly affect the centroid position, most likely associated with the mask machining alignment and optical variations and/or distortion.

3.3.1. Mask Tilt Angle

The analysis of scan-averaged Gaussian centroids for the RefT (Figure 8, upper panel) allows us to clarify various effects that might degrade the accuracy of mask positioning during scans. On the other hand, Figure 7 illustrates the average of the centroid position of the ResT data which reveals the tilt of the mask. Note that a preliminary measurement of it was presented by EADS-Astrium of 0.5 AL pixels. However we find that the mask tilt is around 0.55 AL pixel (i.e., 32 mas on the sky as the difference between the AC positions of spots *A* and *J*).

A more in-depth analysis applies linear fitting to the AL positions of specific reference spot imprints from *A* to *C* to clarify the contribution in the AL direction shift of the spot positions due to the mask.

The mask tilt, i.e., the AL shift between the positions of the stars *A* and *J* along the fitting straight line, is actually slightly larger than the above raw estimate, namely, on the average of the order of 0.611 AL pixels or 36 mas. Besides the linear component of the mask tilt, the AL shift of the spot positions also includes non-linear points that are possibly associated with either an inaccurate mask machining or a field distortion of the optical setup of the experiment.

3.3.2. Opto-mechanical Jitter

The shape of the *Opto-mechanic jitter* is obtained by compensating the spot centroids for the mask tilt from the best fitting straight line of the positions of the first pinholes *A* to *C*; the result is shown in lower panel of Figure 8.

Figure 8(a) shows the trend of individual scan shifts in the AL direction after removing the mask tilt that undergoes an almost "rigid rotation." which is presumably the result of a mechanical yaw as large as 0.14 AL pixel peak-to-valley.

The average of the mask centroid bias (i.e., the AL positional shift presumably associated with the intrinsic mask geometry and/or other repeatable—e.g., optical—distortions of the experimental setup) is illustrated in Figure 8(b) and is obtained by averaging over the number of scans of the Gaussian spot centroids with respect to the average mask tilt results obtained from the linear fit of the positions of reference spots *A* to *C*.

To investigate the repeatability of the AL position of the mask throughout the whole CCN10 campaign, Figure 9 draws the absolute spot positions, averaged over 19 scans, for all the $S = 60{,}000$ irradiated sessions, where the circle, triangle and diamond symbols are related to the DoB = 0, 5 and 10 sessions, respectively, contrasting with the reference session (square character) executed in equivalent nominal illumination conditions. The linear best fit to the averaged positions of stars *A* to *C* in the non-irradiated zone (straight line) is also employed as a distortion free reference; graphs of the irradiated sessions are translated along the vertical axis to superimpose the reference case to allow a straightforward comparison among the different trends.

Figure 9 disentangles some of the effects that make assessment of the CTI centroid bias problematic, the most relevant of which are variation of the mask position over a range as large as two pixels (AL direction) among the considered sessions and progressive change in the trend of centroid positions in the RefT of the best-fit line as a consequence of residual non-linear opto-mechanical distortions of the experimental setup.

4. Radiation-induced Effects

Typically, CCDs for space applications are designed to face space hostile environments where energetic radiation sources generate damages, degrading the CTE performance and

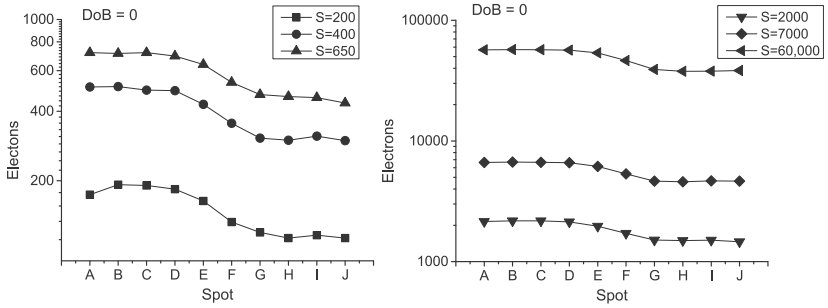

(a) ratio of Gaussian brightness flat-field to the reference case for $DoB = 0$ session: brighter cases, $S \geq 2000$ levels (right); fainter cases, $S \leq 650$ (left)

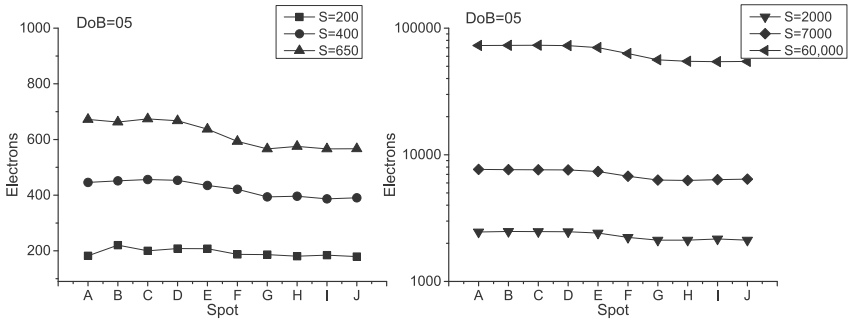

(b) ratio of Gaussian brightness flat-field to the reference case for $DoB = 5$ session. Left panel: fainter illumination levels; right panel: higher brightness levels.

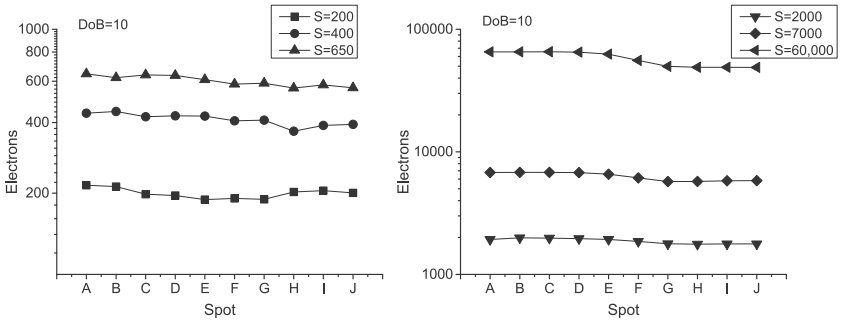

(c) ratio of Gaussian brightness flat-field to the reference case for $DoB = 10$ session. Left panel: fainter illumination levels; right panel: higher source level.

Figure 6. Calibrated brightness distribution achieved through flat-fielding correction for all illumination levels in the diverse RTC sessions with DoB = 0, DoB = 5, and DoB = 10, respectively.

producing displaced silicon atoms, through two different energy dissipation processes associated with ionization energy loss (IEL), and non-ionizing energy loss (NIEL), respectively, called ionization and bulk damages (Janesick 2001). In the case of *Gaia* both IEL and NIEL, the effects are relevant.

4.1. Space Environment

As we have seen in Section 2, the space radiation environmental background interacts continuously with any focal plane assembly. Consequently, our results report what could be long-term cumulative effects of the radiative

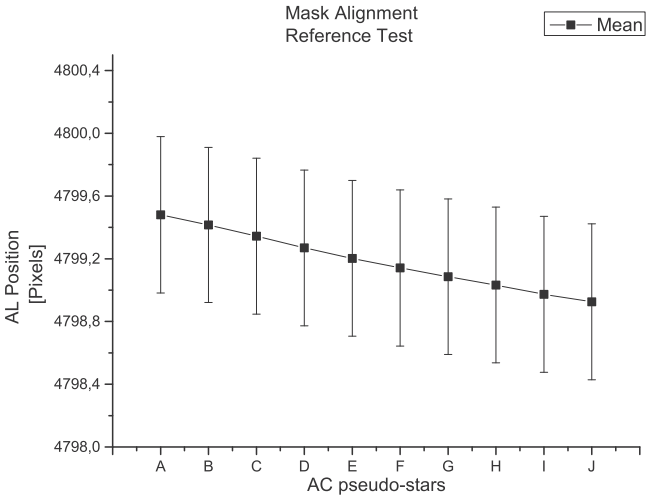

Figure 7. Average centroid positions across the mask for the reference sequence: leading stars from *A* to *J* correspond to holes 2 to 11.

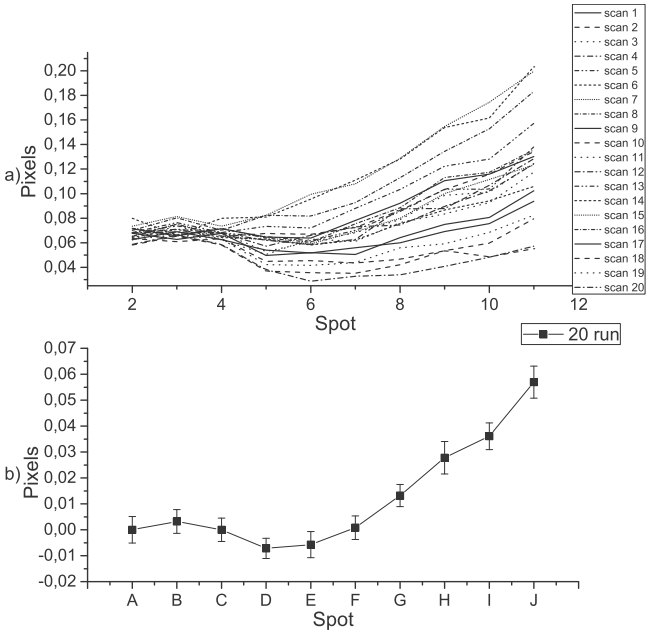

Figure 8. RefT: mask centroid after compensation for the tilt- angle through the centroid position. Upper panel shows the individual scans using the best fitting straight line for the first three stars of the mask and the lower panel shows the average centroid positions of the entire test normalized to the location of star *A*.

environment in L2 of the *Gaia* spacecraft in addition to solar wind based in the RTC CCN10.

FPA is designed and built to face particularly Solar protons; other Energy Particles (EP) such as "Earth-Trapped electrons and protons" are ignored because earth radiation belts do not

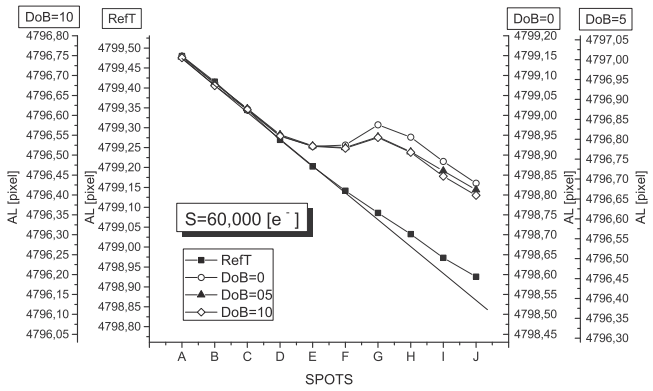

Figure 9. Absolute centroid positions for the RefT and DoB sessions with nominal flux $S = 60{,}000\ e^{-}$. The black straight line represents the nominal mask tilt (i.e., best linear fit calculated from the positions of the centroid measurements of spots *A* to *C* in the reference test). Analogous data reduction of the RefT applies to the RTC test $S = 60{,}000\ e^{-}$, and the best linear measurements from irradiated tests in the NIZ are vertically translated to superimpose the best straight linear fit of the RefT.

reach L2; and Galactic Cosmic Rays (GCR) are ignored due to their small flux like in the case of Heavy Ions (HI).

4.2. Photometric Charge Loss

The RefT photometry session does not allow direct unambiguous measurement of the charge loss at every illumination level; therefore, a recalibration of the sources becomes necessary, using the spots placed on the NIZ of each Irradiated Test as reference points.

From the flat-fielded brightness distribution across the mask (Figures 6(a), (b), and (c)), the average charge loss (due to radiation damage) as a function of the position on the mask (i.e., across CCD areas) is obtained from the difference between the spot intensity and the average signal level of image spots *A* to *C* in the NIZ.

Such an approach leads to the results shown in Figures 10, 11, and 12, which illustrate the absolute and relative amounts of charge loss across the field for all illumination levels and for the different DoB IT.

Note the adoption of a logarithmic scale of the absolute charge loss (Figures 10, 11, and 12, upper panels) so as to better determine the total charge loss trend.

Negative statistical results of the fluctuation analysis of the signal in the non-irradiated region (stars from *A* to *C*), are not representative of the radiation damage effects and are removed from the plot by truncation at the 1 electron threshold. Alternatively, Tables 6 and 7 show the statistical boundary limits of the absolute and relative charge loss for the radiation tests illustrated in Figures 10, 11, and 12, where we can take note of the statistical tendency of belts of DoB effects in the three different CCD zones of the IT (i.e., NIZ, TZ, and IZ). The

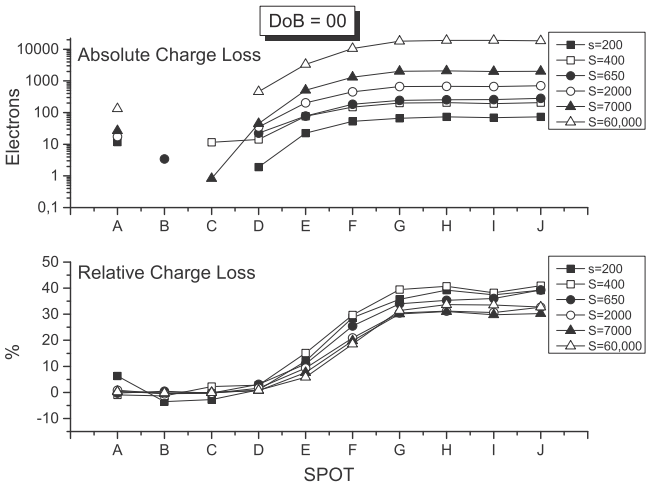

Figure 10. Upper panel: absolute charge loss across the mask for DoB = 0 illumination levels. Lower panel: fractional charge loss using as a reference signal the average from image spots *A* to *C*, transited over non-irradiated pixels. Note that for DoB = 00 about 30% to 40% of the flux is lost; also see Tables 6 and 7, respectively.

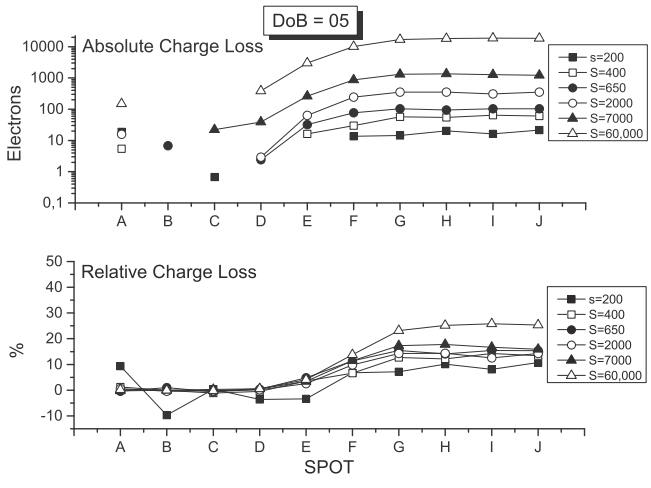

Figure 11. Upper panel: consequence of DoB = 05 over the absolute charge loss for all illumination tests; note that signal performance is less related to DoB = 0. Lower panel: fractional charge loss is distributed over broader ranges for all the tests, between 25% to 10% of the mean flux; also see Tables 6 and 7, respectively.

behavior across the whole CCD is most evident from the fractional charge loss graphs (Figures 10, 11, and 12—lower panels; also see Table 7).

Plots of absolute and fractional charge loss confirm and quantify the very different behavior of the CCD during DoB RTC, which was anticipated qualitatively by the calibrated photometry results in Section 3.2.

The DoB = 0 IT reveals a strong signature of charge loss (see Figure 10); observe that the test measurements at the respective illumination levels of the IT are quite comparable to each other. In the IZ (i.e., stars from *H* to *J*), the fractional charge loss for each illumination level is distributed over the range from 30% to 40% of the average signal of the undamaged stars (*A* to *C*); the dispersion may be related to the measurement statistics. At the same time, the DoB = 5 and DoB = 10 sessions (Figure 11 and Figure 12) illustrate fractional charge loss measurements that are significantly lower than in the null DoB cases, but spread over a wider range from 25% to 10% of the average intensity. Also noteworthy is the change between the DoB = 5 and DoB = 10 IT of the CCD response in the IZ at low illumination levels.

In experiments with the DoB = 10 and illumination levels from $S = 7000$ to $S = 200$, the fractional charge loss drops below a 15% level, and the estimates spread from 15% ($S = 7000$) to 3% ($S = 200$). In particular, for the faintest case of $S = 200$ the trap effect almost disappears and the estimated charge loss in the IZ is negligible, or not significantly different, from the response of the TZ (Figure 12—lower panel).

Conversely, for the brightest signal level $S = 60{,}000$, the charge loss is reduced from ∼35% in the null DoB case to ∼25% in both cases with DoB = 5 and DoB = 10.

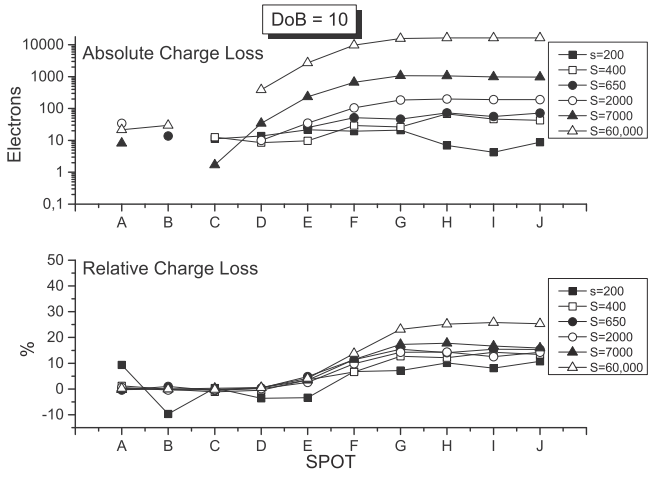

Figure 12. Upper panel: absolute charge loss across the mask for DoB = 10 session radiation test. Lower panel: fractional charge loss under the Influence of DoB = 10 using as a reference signal the average from image spots *A* to *C*; also see Tables 6 and 7, respectively.

Apparently, the DoB seems to provide some compensation for the radiation damage effects on the CTI, which the performance progressively reduces at higher signal levels. The present results provide an estimate of the fractional charge loss as a function of the spot positions on the CCD according to the respective DoB value, which can be compared very well with equivalent evaluations achieved by Short et al. (2005) in an alternative analysis of the same data set.

For the purpose of clarifying the DoB role in mitigation of the radiation damage, as well as providing a simple analytic

Table 6
Statistical Boundary Limits of the Absolute Charge Loss (L = lower, U = upper)

	DoB = 00		DoB = 05		DoB = 10	
Flux	L Bound	U Bound	L Bound	U Bound	L Bound	U Bound
S = 200	18.84822	53.05622	5.987969 e-02	14.38514	4.582046	14.52634
S = 400	57.01893	152.26498	13.71432	42.38618	11.033468	35.37096
S = 650	70.66683	193.25491	27.17609	75.75723	16.682276	48.21981
S = 2000	179.43719	500.64684	84.04401	251.21206	45.355550	137.84285
S = 7000	510.67525	1476.47963	322.5263	946.74133	257.252715	748.49818
S = 60.000	4429.60434	13441.36849	4231.124	12999.40143	3870.391459	11733.75687

Table 7
Statistical Boundary Limits of the Relative Charge Loss (L = lower, U = upper)

	DoB = 00 (%)		DoB = 05 (%)		DoB = 10 (%)	
Flux	L Bound	U Bound	L Bound	U Bound	L Bound	U Bound
S = 200	10.139394	28.54157	0.02981545	7.162685	2.190539	6.944610
S = 400	11.278139	30.11747	3.04044504	9.396954	2.530687	8.112846
S = 650	9.862163	26.97038	4.05876466	11.314386	2.627067	7.593489
S = 2000	8.276353	23.09181	3.40003088	10.162875	2.307160	7.011834
S = 7000	7.675141	22.19060	4.22155153	12.3919 10	3.784165	11.010343
S = 60.000	7.766821	23.56795	5.78442417	17.771650	5.913380	17.927428

description of the trap effect for CTI modeling, we tentatively provide an analytical law relating the charge loss to the signal level, i.e., the size of the charge packet collected in the CCD pixel.

Krause et al. (1999) reports calculations of the charge transfer loss in Scientific CCDs just as illustrated in Figure 13, the average CL as a function of the mean signal for the different DoB sessions. The plots are obtained from absolute charge loss measurements and computing for every illumination level the average CL (y axis) and the mean absolute CL for the three stars H, I, and J in the IZ of the CCD and by employing as the average signal (x axis) the mean calibrated brightness of the three stars A, B, and C in the NIZ (See A_0 of formula 1). A summary of fit statistics of RTC is reported in Table 8, which illustrates the relative calibrated average spot brightnesses in the NIZ vs IZ.

The log-log plot evidences the straightforward relationship between charge loss and signal level and also shows the measurements to be distributed approximately in accordance with the power law $y = aS^b$, where y is the charge loss and S the charge packet size (see Figure 13). The best-fit parameters for such a power law are reported in Table 9 together with associated errors.

Charge loss distribution functions among the different RTC sessions provide helpful hints concerning the possible role of the DoB in mitigating the radiation damage. The increase in steepness seems to be correlated with the increment of the background, while the steepness variation is due to the strong decrease in the charge loss in the case of faintest signals. The

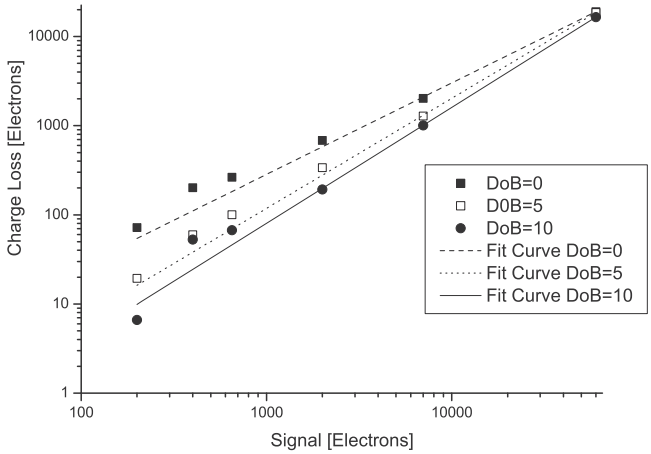

Figure 13. Charge loss as a function of the charge packet size for every DoB session; best-fit curves of the measurements for the power law $y = aS^b$ are also shown.

gap among the curves could be fully attributed to the moderate light background, whose contribution integrated over the *Gaia* 15 × 15-pixel window is estimated to be around 900 and 1800 electrons, respectively, for the DoB = 5 and DoB = 10 cases.

These results seem to confirm the effectiveness of the DoB in partially compensating the radiation damage effect, and that faint sources seem to have a larger relative benefit of such a

Table 8
Summary of Calibrated Brightness Spots in the NIZ vs. IZ

Statistical Parameters	DoB = 0	DoB = 5	DoB = 10
Number of points	6	6	6
Degrees of freedom	4	4	4
Reduced Chi-square	7897, 19333	1419, 57721	325, 67746
Adj. R-Square	0, 99986	0, 99997	0, 99999

Table 9
Parameters of the Power law $y = aS^b$ Best Fitting the Charge Loss Measurements

DoB	Parameter	Value	Error
	a	0.236	0.046
0	b	1, 027	0.018
	a	0.023	0.003
5	b	1, 235	0.013
	a	0.010	0.001
10	b	1, 301	0.008

compensation (which is nonetheless larger in absolute terms for brighter sources).

Nevertheless, taking also into account the temporal succession of DoB = 5 and DoB = 10 tests, performed with a short time elapse between them, and of the earlier DoB = 0 session, performed almost one month earlier (See Table 2), the above fitting functions could also describe different radiation damage states even thought the CCD remains in a cryogenic chamber. However Gow et al. (2015) details the detector performances when CCDs are irradiated under diverse environmental conditions and how these differ. Therefore, the model most appropriate for reproducing the actual response of the damaged CCD should be evaluated in the light of the knowledge of the real CCD operational state during and in between test sessions and with account of the impact it has on the distribution and behavior of the electron traps.

4.3. Astrometric Bias

Concerning the calibration of LSFs and evaluation of the respective CTI centroid bias, the analysis in Section 3.3 provides a way to estimate the compensation of the Gaussian centroids versus the geometric features of the mask tilt distortion as follows:

First, the averages of the Gaussian centroids (i.e., LSFs in AL direction) for each DOB and illumination level are normalized to the average linear trend which is calculated by the positions of the three nominally undamaged spots (i.e., *A* to *C*) independently in each test.
Second, the relative positions are compensated for the average mask centroid bias (described in Section 3.3), which represents the opto-mechanical imperfections as a whole under the reasonable assumptions that the mask is rigid and the optical setup does not change significantly throughout the test sessions.

Figure 14 illustrates the S/N influence over all the scans averaged in AL direction and shifted between the positions of spots *A* to *J* along the mean linear best fit of the non-irradiated positions *A* to *C*. Note as well that the increasing error for the faintest sessions ($S < 600$ electrons) is correlated with the decreasing SNR as tabulated in Tables 3, 4, and 5, respectively.

The results of individual steps of such an approach are shown in Figure 15 separately for different signal levels and DoB. Note that the mask bias (see Section 3.3, Figure 8) is also shown as a square symbol over the bold line, displaying the position shifts after compensating for the mask bias whereas Figure 16 shows the centroid positions corrected for the mask tilt.

The consequences of radiation damage suffered by the CCD and shown through the LSF position shift across the irradiated zone and transition zone are already evident once the mask tilt is compensated for. However, further removal of the opto-mechanical distortion, i.e., mask bias (see Figure 8), is decisive for accurate quantification of the centroid shift linked to the CTI effects.

After compensation for both components of mask geometric features (i.e., tilt and distortion), the CTI centroid bias (Figure 16, position residual associated to the radiation-induced CTI effects) progressively increases from an almost null value, for spots *A* to *C* in the NIZ, to a quasi-constant value for spots *H* to *J* in the 4×10^9 IZ, where the position residual depends on the illumination level: the brighter the source, the larger the position shift.

Such a trend is very well defined for all the brighter sessions ($S \geqslant 2000$); for the fainter sessions ($S \leqslant 650$), the LSF position shift measurements in the irradiated region scatter over a range as large as 0.1 AL pixels as a result of both the mask positioning error (Section 3.3) and the reduction of SNR that affect the centroid estimates (Figure 14).

A comparative analysis of sessions with different DOB levels in Figure 15 reveals that the moderate DOB levels, 5 and 10 electrons per pixel, actually provide a detectable mitigation of the position shift associated to the radiation damage, in particular, for the cases of source brightness $S \geqslant 2000$, for which the addition of DOB produces a significant reduction, correlated with the DOB value of the position shift in the irradiated region of the CCD (compare Figures 15 and 16).

For the measurements at low-source brightness (i.e., $S \leqslant 650$), the DOB role in partially compensating the CTI centroid bias is not so evident as for the brighter cases, likely as a result of the inaccuracy affecting the centroid estimates for

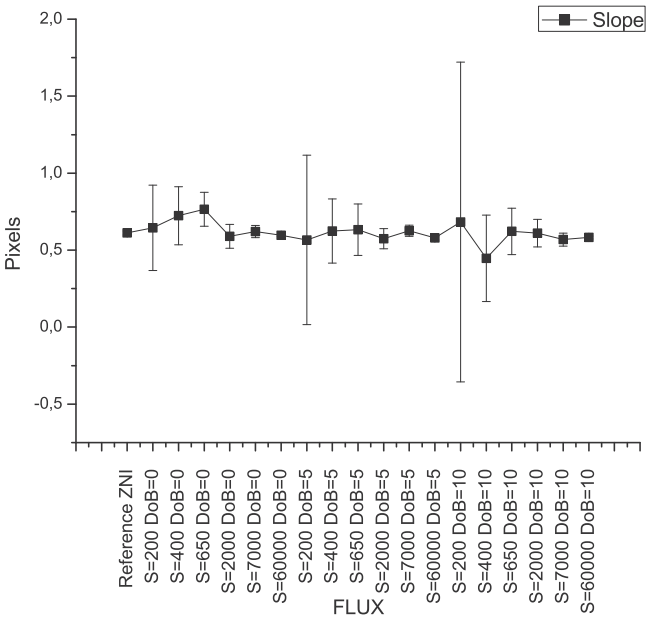

Figure 14. Mask tilt observation in the RTC CCN10 potentially influenced by the contribution of DoB S/N at each test.

fainter sources dominated by additional noise from the background signal (see Figure 14).

Only the sessions with $S = 650$ manifest an evident mitigating role of the DOB, which, independently of the applied signal intensity of either 5 or 10 electrons/pixel, is capable of recovering almost the whole amount of the positional shift affecting the spots D to H placed at the irradiated area of the CCD.

To clarify the usefulness of the DOB for the CCN10 RTC, it is convenient to represent the estimated centroid bias as a function of the source intensity for each adopted DOB configuration.

The relationship between the centroid bias and the signal brightness (Figure 17) is obtained by comparing the LSF positional shift (Figure 16), corrected for the locational effects of the opto-mechanic setup, with the average non-irradiated signal brightness from the photometric analysis (Section 3.2). The relation between the radiation-induced LSF position shift and the signal brightness can be split into two signal regimes. For the fainter signal regime, $S \leqslant 650$, the position shift undergoes a steep decrease as the signal increases; such a trend seems well defined for the measurements with DoB = 0 and DoB = 10.

Potential mitigation of the CTI effects by the DOB is revealed by a noticeable gap of the order of 0.02 AL pixels, almost constant along the considered signal range between curves for sessions with null DOB and DoB = 10.

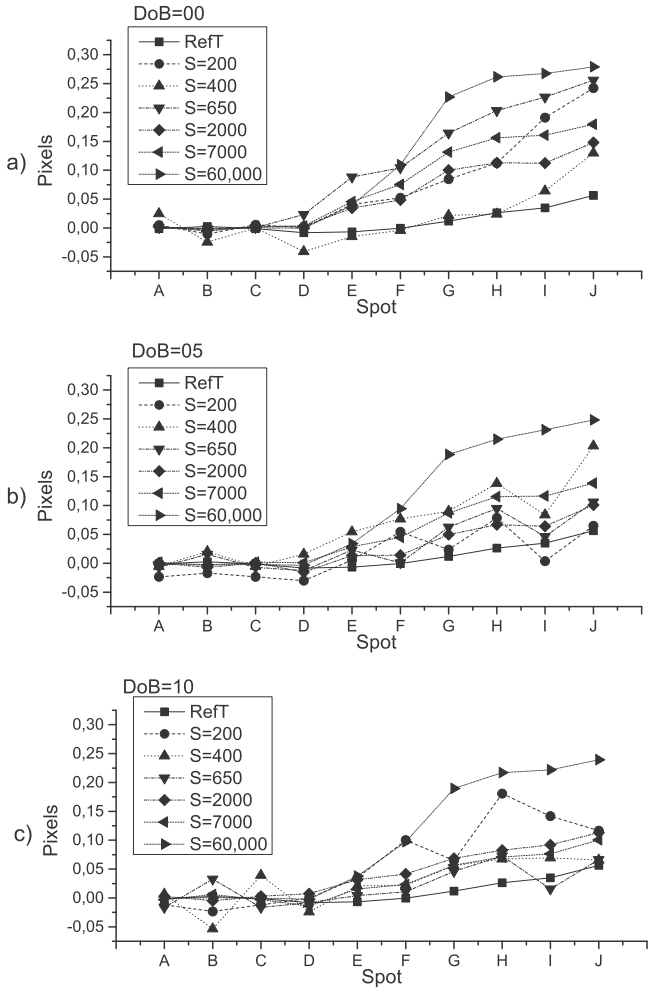

Figure 15. Average centroid bias across the mask as measured during the various DOB sessions and RefT (black squares) which represents the mask distortion; the different tests are compensated for by the mask tilt.

Unfortunately, measurements with DoB = 05 depart from the trend observed for the other DOB cases, presumably because of some unpredictable opto-mechanical changes in the experimental setup which perturb the centroid estimate, and are not compensated for by the adopted data processing approach. The discrepancy makes any conclusion very preliminary.

For brighter signal regimes, $S \geqslant 2000$, the centroid bias is well correlated with the signal intensity, and the shift amplitude apparently scales proportionally with the logarithm of the source brightness. In this signal range, the addition of a moderate signal background (DoB = 05-RTC), leads to a reduction of the shift by an amount of the order of 0.05 AL pixel (≈3 mas) almost constant over the brighter signal range.

Increasing the DOB level by 10 e^-/pixel, we observe a healing effect in the case of $S = 7000$ (Figure 17) where the

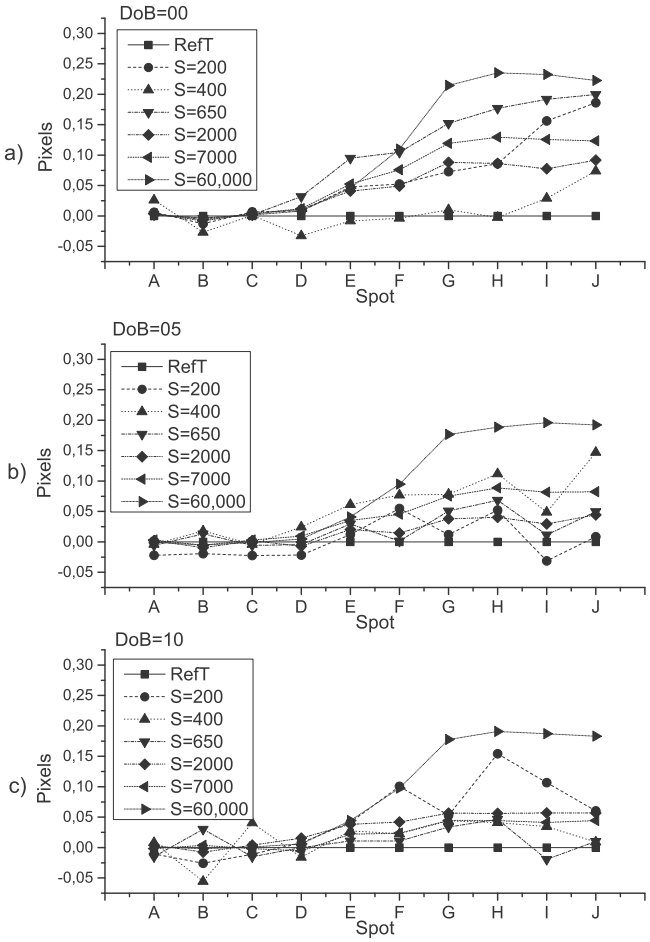

Figure 16. Average centroid bias compensated for mask distortion.

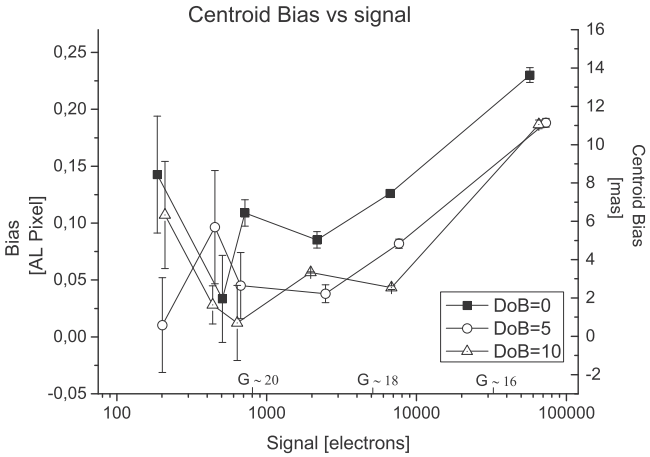

Figure 17. Average centroid shifts of the irradiated spots (*H* to *J*) vs. the average brightness of non-irradiated spots (*A* to *C*) for different DoB sessions: the position shift is shown in AL pixels (left vertical axis) and mas (right vertical axis). Error bars show the bias rms computed over the number of mask passages performed in each test session.

role is detectable and the mitigation of the Astrometric bias improves with respect to the DoB = 05 case. On the other hand, at $S = 600{,}000$ in the DoB = 5 and 10 cases the contribution does not change too much with respect to partial mitigation in the Astrometric bias.

It is worth noting how the change from negative to positive steepness of the CTI centroid bias curves seems to occur at an integrated signal value very close to the saturation level—quoted as large as 1800 electrons—of the supplementary buried channel (SBC), which is implanted in the *Gaia* CCD pixel so as to improve the radiation hardness of the device. The observed behavior of the CTI centroid bias could be tentatively accounted for in the light of such a complex *Gaia* CCD pixel architecture. Small charge packets, up to 1800 e^- in size, are fully transported through a narrow stream confined to the SBC. The traps in the reduced volume of SBC get almost completely filled at a relatively low signal and, consequently, the centroid bias decreases as the charge packet increases, until reaching the minimum when the pixel begins to operate close to the SBC saturation mode.

As the photon charge packet size exceeds the SBC saturation level, the charge excess uses a larger portion of the regular buried channel, and in turn, an increasing by a larger number of traps, which are responsible for the LSF position shift increase in the brighter signal regime. For the sake of comparison, Figure 18 shows the relation between centroid bias and signal intensity obtained by independent analyses carried out on the same data set by Short et al. (2005) and Brown & Van Leeuwen (2008).

Our estimates of the CTI centroid bias basically confirm the behavior reported by Short et al (2008). In particular, when results from similar fitting curves are considered (Figure 18, black box and black circle), our analysis compares well with Short's over the whole interval of the considered signal intensities. Comparison with Brown & Van Leeuwen results (Figure 18, white box) is more problematic.

Both analyses provide comparable estimates of the CTI centroid bias for the brighter sources ($S \geqslant 2000$), but they differ significantly in reproducing the centroid bias in the low signal regime for $S \leqslant 600$. Brown's analysis yields a very high value of the positional shift for the fainter sources, which seems to suffer a shift as large as that experienced by the brightest sources, i.e., $S = 60{,}000$.

Furthermore, and very unexpectedly, Brown's measurements with DoB = 10 yield a negative bias value for the fainter sources, compatible with the LSF leading edge distorted by a charge excess. This may be explained by the different methods for normalizing and correcting systematic errors.

5. Conclusions

All CCN10 RTC were executed in adequate S/N regimes where the measurements exhibit a S/N larger than the

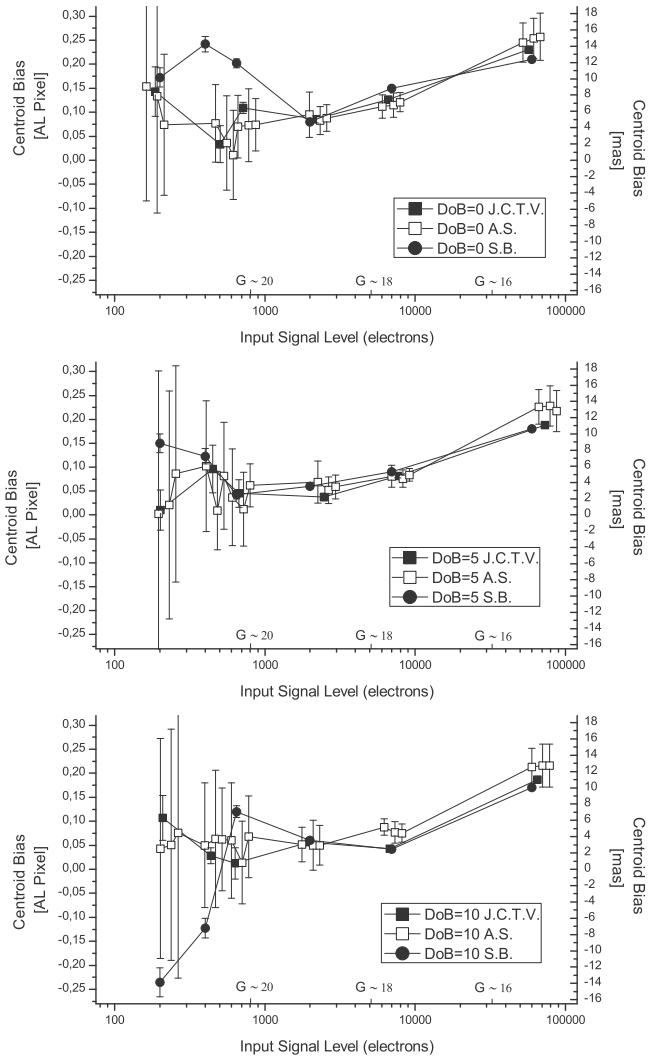

Figure 18. Bias from independent analyses of CCN10 campaign, arranged in increasing order of the DoB level from top to bottom: our results are shown in black boxes; the white squares indicate the results of Short et al. (2005, Figure 6) obtained by Gaussian fitting of the CCN10 data; full circles are for data from the Brown & Van Leeuwen (2008, Figure 19).

detectability threshold (e.g., $S/N > 3$) in almost all cases. The radiation damage effects are clearly shown by the evolution along the transits of image spot brightness across the irradiated area.

Charge loss due to the presence of traps affects the simulated star signal mostly at the first transit; a further, less intense, charge loss can occur at the second transit, after that transit a small fraction of traps reveals a large de-trapping time constant as can be seen in Figure 5(b). Such a behavior indicates that the traps involved are very effective in capturing electrons and less so in releasing them (i.e., they are slow traps), their release time constant is longer than the interval between transits (30 s). Theoretically, photon packets are trapped thanks to energy levels created in the semiconductor band gap because the damage is caused by high energy protons which displace atoms from their CCD silicon lattices.

The average charge loss is highly correlated with the signal intensity, in accordance with theoretical predictions that relate the trap behavior (e.g., time capture constant) to the electron density in the pixel. Unfortunately, the large and unexplained discrepancy in the CCD response in different test sessions does not allow identification of a simple analytic dependence of the charge loss upon the integrated signal capable of reproducing the behavior of the damaged CCD (i.e., having experienced a radiation dose equivalent to the expected *Gaia* end-of-mission level, i.e., 4×10^9 protons/cm^2).

The current results only allow to state that the charge loss measurements follow a power law $y = aS^b$ (Figure 13) whose parameters may vary over large ranges. As a possible consequence of DoB variation over the CCD operational parameters; the large spread involved points to the need for a careful assessment of the actual analytic model of charge loss, based on a much better knowledge of the real experimental conditions and possible changes imposed on the detector.

The adopted levels of DoB contribute partially to mitigating the radiation damage, and the benefit in terms of the decrease in the charge loss is particularly evident in the case of faint signal levels. This also suggests that an appealing alternative to DoB for trap filling and mitigation of radiation damage effects is CI, performed at a comparably low rate (e.g., once every several minutes), with an intensity parallel to the high end of the detector dynamic range.

The centroid analysis demonstrates that the CCN10 RTC was executed with a rather loose control of the mechanical positioning of the mask (Figure 8(a)). The large mask initial position jitter (as large as 0.5 AL pixels rms) and the mechanical yaw (of the order of 0.04 AL pixel rms) makes the LSF location measured in the RefT session unreliable as a reference position for assessing the CTI-induced position bias. The most relevant information, useful for the centroid bias calibration, that the non-irradiated session can provide, is the amount of intrinsic mask distortion, Figure 8(b) (i.e., the contribution to the LSF position shift due to both the mask machining and residual optical distortions). This can affect the LSF location by shifts as large as 0.06 AL pixel at the maximum extent corresponding to the spots in the 4×10^9 IZ.

Once the irradiated LSF positions are properly compensated for the actual mask geometric bias (i.e., tilt and distortion), the centroid residuals provide a reliable estimate of the position bias associated with the radiation damage, i.e., the CTI-induced astrometric bias.

In general agreement, the correlation of the measured CTI centroid bias with the calibrated brightness proves that the addition of a moderate DoB is a viable solution for mitigating the CTI effects in the brighter signal regime ($S \geqslant 2000$). The

DoB = 05 e^- per pixel provides a noticeable reduction, of the order of 0.05 AL pixel (≈3 mas), of the position shift, but the increase in the background signal, up to 10 electrons per pixel, apparently does not give any further improvement.

The analysis performed for the centroid bias at low signal levels (i.e., up to values comparable with the quoted saturation level)—1800 e^-—of the SBC, demonstrates the effective role of the SBC in hardening the CCD against the radiation-induced CTI effects for the faintest signals (see Prod'homme et al. 2011). Unfortunately, the lack of measurements with a source power in the range between $S = 650$ and $S = 2000\,e^-$ does not allow to definitively clarify the role of the SBC, in terms of the achievable astrometric accuracy in the presence of radiation damage, for signal intensity close to the expected *Gaia* limiting magnitude $G = 22$, i.e., ≈810 $photo - electrons$.

This work was supported by the Italian Space Agency (ASI) under contracts: $I/058/10/10$ and $2014 - 025 - R.1.2015$.

JCT is supported by CONICYT-Chile, under grant FONDECYT # 3150598.

Additional support was provided by the Advanced Center for Electrical and Electronic Engineering, Basal Project *FB*0008.

The authors thank the anonymous referees for all the suggestions and comments that greatly improved the original manuscript.

References

Bebek, C. J., Groom, D. E., Holland, S. E., et al. 2002, Proc. SPIE, 4669, 161
Brown, S., & Van Leeuwen, F. 2008, Analysis of the CCN10 data set: CTI effects on a *Gaia* astrometric CCD, Internal *Gaia* livelink, GAIA-CH-TN-IOA-SWB-001-3
Corcione, L., Terrazas, J. C., Lattanzi, M., et al. 2009, CCN10 radiation test campaign data: photometric performance and charge loss in *Gaia* irradiated AF CCD, nternal *Gaia* livelink, GAIA-C3-TN-INAF-LC-001-0
Crowley, C., et al. 2016, A&A, 595, L2
Daibog, E., Kecskemety, K., & Logachev, Y. 2013, Journal of Physics: Conf. Ser., 409, 012162
de Bruijne, J. 2016, List of *Gaia* acronyms, https://gaia.esac.esa.int/gpdb/glossary.txt
ESA/Gaia 2017, Spacecraft & Instruments, https://www.cosmos.esa.int/web/gaia/focal-plane
Fusero, F., et al. 2007, *Gaia* Radiation Analysis Report, EADS Astrium, GAIA,ASF,TCN.SAT.00035
Gaia Collaboration, Prusti, T., de Bruijne, J., et al. 2016, A&A, 595A, 1G
Gow, J. P. D., Smith, P. H., Pool, P., et al. 2015, JInst, 10, C01037
Hopkinson, G. R., & Mohammadzadeh, A. 2003, ITNS, 50, 1960
Janesick, J. R. 2001, Scientific Charge-Coupled Devices, Vol. PM83 (SPIE Publications)
Krause, N., Briel, U. G., Dennerl, et al. 1999, Proc. SPIE, 3765, 220
Meidinger, N., Strüder, L., Holl, P., et al. 1996, NIMPA, 377, 298
Mendez, R. A., Silva, J., Orostica, R., et al. 2014, PASP, 126, 798
Pasquier, J. F., et al. 2011, Radiation campaign #5 tests plan, EADS—Astrium, Internal *Gaia* livelink, GAIA.ASF.PLN.00097
Perryman, M. A. C., de Boer, K. S., Gilmore, G., et al. 2001, A&A, 369, 339
Prigozhin, G. Y., Kissel, S. E., Bautz, M. W., et al. 2000, Proc. SPIE, 4140, 123
Prod'homme, T., Brown, A. G. A., et al. 2011, MNRAS, 414, 2215
Prod'homme, T., Holl, B., Lindegren, L., & Brown, A. G. A. 2012, MNRAS, 419, 2995
Raison, F., & Martin-Fleitas, J. 2009, Trapping the traps in *Gaia* CCDs, Ist EIRO forum School of Instrumentation, https://indico.cern.ch/event/43007/contributions/1065037/attachments/927923/1313791/Poster_TrappingTheTrapsInGaiaCCDs_Fred_Juanmadf.pdf
Seabroke, G. M., Holland, A. D., Burt, D., & Robbins, S. 2009, Proc. SPIE, 7439, 743905
Short, A., Hopkinson, G., Laborie, A., et al. 2005, Proc. SPIE, 5902, 31
Short, A., Prod'homme, T., Weiler, M., Brown, S., & Brown, A. 2010, Proc. SPIE, 7742, 774212
Terrazas, J. C., et al. 2010, Astrometric performances of *Gaia* irradiated AF CCD from CCN10 radiation test campaign data analysis, Internal *Gaia* livelink, GAIAFPA.RPT.00700.T.ASTR
Walker, A., Eaton, T., Steward, R., et al. 2008, Proc. SPIE, 7106, 71061H